Implementation of a hyperspectral integrated vision system combining radar technology and single-pixel optical principle for unmanned ground vehicles (UGV)

C. Osorio Quero*, D. Durini, R. Ramos-Garcia,
J. Rangel-Magdaleno, J. Martinez-Carranza, J. L. Olvera, A. Corona

National Institute of Astrophysics, Optics and Electronics (INAOE)
Luis Enrique Erro 1, 72840 Tonantzintla, Puebla, Mexico
*caoq@inaoep.mx

ABSTRACT

During the last decades the *radio detecting and ranging* (RADAR) technology underwent an evolution transiting from the linear-frequency-modulated (LFM) systems developed in the 1970s, up to the orthogonal frequency-division multiplexing (OFDM) systems developed in the early 2000s. In mid 2010s, systems were proposed that combined the radar principle with optical solutions developed for imaging and ranging tasks following a hyperspectral embedded systems approach. The idea was to profit on the one side from the possibility offered by RADAR systems to work in harsh environments using emitted radio waves and detect mainly metal objects placed far away (hundreds of meters or even kilometers) from the detection system with positioning spatial resolutions in tens of centimeters, even if there are non-metallic barriers such as e.g. walls in between; and expand this possibility by using optical systems (e.g. *light detecting and ranging* –LIDAR- systems), using visible light active illumination, capable of generating 2D and 3D images of objects placed at much smaller distances from the detector, but allowing for much higher spatial resolutions (in the millimeter range). To reduce the atmospheric absorption of the emitted active illumination and increase the emitted optical power allowed for these systems that can correctly function even in harsh environments, we propose shifting the active illumination wavelengths from the visible range to the near infra-red (NIR) range, e.g. to 1550 nm. Lacking affordable image sensors fabricated in InGaAs technology, capable of detecting NIR radiation, in this paper we propose a hyperspectral imaging system using a very low power consuming single commercially available InGaAs photodiode to generate 2D images using the single-pixel imaging (SPI) approach based on compressive sensing (CS) and an array of NIR light emitting LEDs, combined with an 80 GHz millimeter band RADAR. The system is conceived to deliver a maximum radar range of 150 m with a maximum spatial resolution of $\leq$ 5 cm and a RADAR cross-section (RCS) of $10 - 50$ m^2, combined with an optical system capable of generating 24 fps video streams based on SPI generated images yielding a maximum ranging depth of 10 m with a spatial resolution of < 1 cm. The proposed system will be used in unmanned ground vehicle (UGV) applications enabling decision making in continuous time. The power consumption, dimensions and weight of the hyperspectral ranging system will be adjusted to the UGV targeted applications.

Keywords: Millimeter Radar, single-pixel imaging (SPI), infrared, 2D radar imaging, unmanned ground vehicle (UGV), hyperspectral imaging, time-of-flight (ToF) 3D imaging and ranging

1. INTRODUCTION

Throughout the last several decades, many different methods have been proposed that enabled *radio detecting and ranging* (RADAR) imaging, based mostly on Linear Frequency Modulation (LFM) [1] of radiofrequency signals using fixed bandwidths on the one hand, and the Orthogonal Frequency Division Multiplexing (OFDM) [2] on the other. In mid 2010s, systems were proposed that, following a hyperspectral embedded systems approach [3], combined RADAR with optical solutions developed for imaging and ranging tasks based mainly on time-of-flight (ToF) [4, 5], still a very attractive option for autonomous driving and similar applications in UGVs or even *unmanned flying vehicles* (UFVs or drones), where these systems are used to increase the navigation capability and collision prevention. Vision systems such as LIDAR (*light detection and ranging*) [6], ToF-based systems using highly sensitive photodetectors and sophisticated scanning mechanisms, must still be improved to enable correct depth definition for the objects present in the scene of interest if under harsh environment conditions (rain, snow, fog, smoke, etc.) and increase the robustness of these systems for real outdoor scenarios. Namely, the main drawbacks when dealing with ToF based systems such as LIDAR are: (1) the levels of background illumination (that could reach 100,000 lux) and the photon shot noise related to it that defines, added to the electronics read noise, the noise-floor for these kind of system developments; (2) the maximum amount of optical power, which if increased can be used to overcome the background illumination noise level issues, allowed to be used for active illumination in these systems defined by the international *Eye Safety Regulations* [7] and the *maximal permissive exposure* (MPE) associated with them [8]; (3) the maximum depth of the objects in the scene of interest that can be detected with the system, which depends on the atmospheric absorption coefficient [9] at the wavelength chosen for active illumination, the reflection coefficient of the objects in the scene at that wavelength, and the amount of micrometer size particles (rain, snow, fog, smoke, etc.) present in the system causing different types of light scattering events; and (4) the electromechanical complexity and reliability of the LIDAR scanning mechanism. As reported in [8], the maximum optical power permitted for active illumination, expressed in J/m^2 in terms of MPE, can be increased by more than four orders of magnitude for illumination pulses of some tens of nanoseconds (normally used in ToF applications) if the active illumination wavelength is shifted from the normally used 850 nm to 1550 nm. Furthermore, as reported in [9], the absorption by water dimers present in the atmosphere decreases significantly for the same wavelength shift allowing for a higher amount of radiation reflected by the objects in the scene to reach the photodetector of a ToF based imaging and ranging system. Silicon based ToF systems [4, 5] use single photodetectors or arrays of specially designed pixel architectures for the tasks described. The main problem is that due to the silicon energy gap (of 1.1 eV for indirect electron transitions [10]), these silicon photodetectors or image sensors have quantum efficiencies of far below 10 % in the NIR part of the spectra, and cease to generate electron-hole pairs all together at the cut-off frequency corresponding to the 1127 nm wavelength. The commercially available alternative are InGaAs photodetectors with very acceptable optical sensitivities in the range between 900 nm and 1600 nm [11] wavelengths; a property that additionally convert them in high-pass sensing filters, cutting off the background radiation in the wavelength range below 900 nm. Unfortunately, image sensors fabricated in this technology are not commercially available or are very costly, which leaves using single photodetectors as a feasible option for the tasks described applying the single-pixel imaging (SPI) algorithms [12] based on the *compressive sensing* (CS) [13] approach.
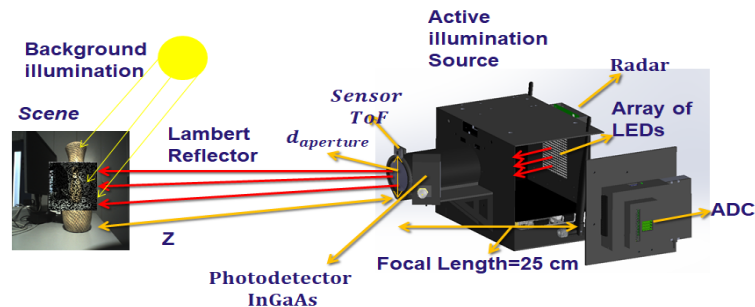

Figure 1. Schematic representation of the SPI based imaging system proposed in this work, showing the array of emitting LEDs illuminating the scene of interest, the background illumination present in that same scene, the objects in the scene behaving as Lambert reflectors of the active illumination used, and finally the InGaAs based single photodetector (or a line sensor) placed aside the array of LEDs used to detect the radiation reflected by the objects in the illuminated scene through a Fresnel lens.

The SPI uses a series of specially designed illumination patterns (e.g. *Hadamard* patterns [12]), generated by an array of light emitters such as LEDs (see Fig. 1) or an array of specially designed micro-mirrors illuminated by a single source, that are projected to illuminate the scene of interest, get reflected by the objects situated in this scene, and finally be detected by the single photodetector placed aside. A two-dimensional (2D) image can be reconstructed from the electrical response levels delivered by the single photodetector used in the system to each of the projected illumination patterns, using a scarce number of these patterns and e.g. the Orthogonal Matching Pursuit (OMP) [14] approach. Commercial LIDAR systems normally use a scanning frequency of 2.5 kHz [6] and are used to detect single points, line scans or 2D images with low spatial resolutions. If a targeted 2D image to be formed by a LIDAR system with a said scanning frequency is to consist of 64×64 pixels, the image acquisition time of approximately 1.6 s would be required, definitely too long if the system is to be used for decision making in continuous time for a moving UGV or UFV. If instead the SPI approach using OMP is followed, the acquisition time required to generate the same quality image would be of between 10 and 200 ms for the acquisition of the generated illumination patterns, and additional 25 ms for signal processing and image generation. So, we propose a hyperspectral ranging system that uses a line sensor made of 1×1024 single commercially available InGaAs photodiodes to generate 2D images using the single-pixel imaging (SPI) approach based on compressive sensing (CS) and an array of NIR light emitting LEDs with emission wavelength of 1550 nm, all combined with an 80 GHz millimeter band RADAR.

2. MODEL DEVELOPED FOR THE SPI SYSTEM PROPOSED

As shown in Fig. 1, we are proposing an SPI system consisting of an array of emitting LEDs used to illuminate the scene of interest, where the objects in the scene behave as Lambert reflectors of the active illumination used, and an InGaAs photodetector placed aside the array of LEDs that is used to detect the radiation reflected by the objects in the illuminated scene and collimated by a Fresnel lens. We decided to use an array of 16×16 EOLD-1550-525 InGaAs/InP NIR LEDs [15] yielding maximum individual radiant intensity of 11 mW/sr, considering 100 mA biasing, at a peak wavelength of 1550 ± 20 nm with a viewing angle of 20° and a LED switching time of 10 ns. The latter translates in a combined radiant intensity of the LED array of around 2.8 W/sr. In the proposed configuration, we considered using the narrow band-pass filter for 1550 ± 6 nm wavelengths [16] covering the photodetector. To be able to assess the amount of photons generated by the NIR LED array reaching the different objects in the illuminated scene, being reflected by them, and finally impinging the photoactive area of the InGaAs photodetector located aside the LED array, we considered the Lambert reflection model, the background illumination generated photon shot noise (PSN) that follows the *Poisson* probability distribution function, and different reflection coefficients of the objects in the scene, as well as different distances of these objects from the photodetector. Considering the background illumination to be of 100 klux in photometric units (1 lux = 1 lm/m^2) following the sun spectra, the first task is to determine the photon flux density in radiometric units of W/m^2 for the wavelength range defined by the narrow band-pass filter used. Considering the radiant flux $\Phi(\lambda)$ emitted by the sun, proportional to the area enclosed by its known sun spectral distribution curve, in order to express it in terms of irradiance (in W/m^2) it must at first, as expressed by Eq. (1) [17], be transformed into a luminous flux (measured in lumen) by multiplying it by the photopic relative luminous efficiency function $V(\lambda)$ [17] and the maximum luminous efficacy factor $K_m = 683$ lm/W [17]. In the case of interest, $\lambda_{max} = 1556$ nm and $\lambda_{min} = 1544$ nm.

$$E_{e\_sun}(\lambda) = \int_{\lambda_{min}}^{\lambda_{max}} \Phi(\lambda)V(\lambda)d\lambda \qquad (1)$$

A key factor here is the assessment of the minimum charge-collection or radiation integration time T_{int} required by the chosen photodiode to generate an electrical signal higher than the electrical noise floor under different working conditions, i.e. the minimum time required to capture an amount photons emitted by the array of LEDs, reflected by the objects in the illuminated scene, and finally converted into electrical signals by the photodetector that is higher than the electrical noise floor generated by the background illumination added to the read noise. Eq. (2) [18] models the photon energy (in Joules) arriving at the photodetector and considers the band-pass filter situated in front of the chosen photodiode, the detector quantum efficiency QE(λ) in this bandwidth, the integration time T_{int}, and the photodetector effective photosensitive area defined as $A_{pix} = A_{HxW} \cdot FF$, where A_{HxW} is the photodetector window area and FF the fill-

factor of each pixel. Additionally, Eq. (2) takes into account the background (sun) irradiation level $E_{e\_sun}(\lambda)$ at the bandwidth defined by the band-pass filter calculated for the bandwidth of interest using Eq. (1) [18], as well as the maximum irradiance emitted by the active illumination source (the NIR LED array) $\Phi_{e\lambda}$, the material reflection indices ρ of the objects in the illuminated scene, as well as on the distance z of these object to the photodetector (see Fig. 1). In Eq. (2) [18], the focal number $f_\#$ is defined as the ratio between the focal distance and the aperture distance of the lens placed in front of the photodetector ($f_\# = f_{foc} / d_{aperture}$), τ_{lens} is the lens transmittance coefficient, α_{FOV} the focal aperture field-of-view angle of the emitting LED array, h is the Planck constant, c the speed of light, and $\Delta(\lambda - \lambda_2)$ for $\lambda_1 < \lambda < \lambda_2$ is the proportional factor introduced to compensate for deviation of the actual irradiation wavelength used in the system with respect to λ_2.

$$E(N) = \int_{\lambda_{min}}^{\lambda_{max}} \frac{\rho \tau_{lens} QE(\lambda) T_{int} A_{pix} FF \lambda}{4hcf_\#^2} \left[\frac{\Phi_{e\lambda} T_{int} \Delta(\lambda - \lambda_2)}{\pi z^2 \tan(\alpha_{FOV})^2} + E_{e\_sun}(\lambda) T_{int} \right] d\lambda \qquad (2)$$

Taking into account the mean energy of a single photon, expressed in eV, within the bandwidth of $\Delta\lambda = 1550 \pm 6$ nm of the narrow band-pass filter used (calculated as $E_{ph} = 1.24 / \lambda$, for $\lambda = 1.55$ μm [10]), the average amount of single photons arriving at the photodetector can be expressed in terms of Eq. (3). Following the *Poisson* distribution function, the photon shot noise $\overline{n}_{ph}$ expressed in terms of the statistical variation of arriving photons holds a square root relation to n_{ph} and can be expressed as shown in Eq. (4). The two additional terms that must be considered to evaluate the overall system noise are the so called dark shot noise $\overline{n}_{dark}$, i.e. the statistical variation of thermally generated electrons within the photodetector material that due to the *Poisson* probability distribution obeys the same square root relationship to the mean amount of thermally generated electrons (dark current) n_{dark}, and the read noise $\overline{n}_{read}$ produced by the different physically caused statistical variations of the amount of electrons flowing in the readout circuit of the system.

$$n_{ph} = E(N) / E_{ph} \qquad (3)$$

$$\overline{n}_{ph} = \sqrt{n_{ph}} \qquad (4)$$

Finally, the overall system noise floor can be expressed, as shown in Eq. (5), in terms of the sum of squared variances ($\sigma = \overline{n}^2$) for these three elements: the photon shot noise, the dark shot noise and the read noise.

$$\sigma_{total} = \sqrt{\left(\sigma_{ph}\right)^2 + \left(\sigma_{dark}\right)^2 + \left(\sigma_{read}\right)^2} \qquad (5)$$

Considering the overall SPI system, we decided to carry out a comparative study between three different types of InGaAs photodetectors, namely:

1. *Hamamatsu* G9201-256SB [19] one-stage cooled 256 × 256 pixel InGaAs image sensor with a pixel size of 25 × 25 μm² and the image size of 3.2 mm², a dark current of 2 – 10 pA if biased at 5V, and integrated with a CMOS charge amplifier array, a correlated double-sampling (CDS) circuit, an offset compensation circuit, and a shift register and a timing generator, yielding a dynamic range of almost 85 dB, typical photosensitivity of 0.95 A/W at the peak wavelength of 1.6 μ, and operating with a maximum output operation frequency of 4 MHz
2. *Hamamatsu* G10768-1024D [20] non-cooled 1024-pixel InGaAs line-sensor with a pixel size of 25 × 100 μm, i.e. a joint photoactive area (image size) of 2.56 mm², and a dark current of 1 – 5 pA if biased at 5V, integrated with CTIA (capacitive transimpedance amplifiers) that allow signal readout at a maximum line rate of 39,000 lines/s achieved through 8 output ports
3. *Thorlabs* FGA015 [21] non-cooled single circular InGaAs photodiode with an active area diameter of 150 μm

(pixel or size of 0.07 mm^2), a maximum optical sensitivity of 0.95 A/W at the peak wavelength of 1.55 µm, a typical dark current of 0.5 nA at a bias voltage of 5 V, and a permitted maximum optical power of 10 mW.

At first, we evaluated the photon shot noise generated by background illumination (glare sun) of 100 klux for the bandwidth of interest, defined by the narrow band-pass filter lens of 1550 ± 6 nm wavelengths [16] as described above, and added this to the dark shot noise calculated considering the dark currents reported in the respective data sheets of the three different photodetectors listed above, finally adding the additional readout electronics read-noise to the equation.

Furthermore, we defined three different reflection coefficients for the materials forming the assumed objects in the scene, namely: 20 % (almost completely dark object), 50 % (half reflecting), and 80 % (almost completely reflecting object); and considered the optical power emitted by 16×16 EOLD-1550-525 InGaAs/InP NIR LEDs [15], described above, emitting approximately 2.8 W/sr with a viewing angle of 20° per single LED including their own photon shot noise in the mix. The final step in the detector system evaluation was to determine the minimum T_{int} required by the system to generate a signal higher than the noise-floor signal (the sum of all described noise mechanisms) in each single pixel, considering here that the photoactive pixel area for the pixels belonging to the first sensor is of 625 µm^2, 2,500 µm^2 for the case of the second sensor, and finally 70,683 µm^2 for the third one. As it can be observed in Table 1, each individual pixel of the first *Hamamatsu* G9201-256SB [19] image sensor manages to surpass the noise-floor voltage signal, in case the reflection index of the object is of $\rho = 80$ % and the object is situated at a maximum distance of $d_{max} = 9.4$ m, within a minimum integration time of $T_{int\_min} = 2.2$ ms. In case the reflection index drops to 50 %, the maximum measurable distance drops down to 4.3 m and $T_{int\_min} = 1.5$ ms. In the worst case scenario, if ρ is only 20 %, $d_{max} = 1.8$ m, although $T_{int\_min} = 900$ µs. These conditions change under different background or active illumination conditions, of course. As expected, the sensor with pixels (or a single pixel, as it results) with the biggest photoactive area (option number 3, *Thorlabs* FGA015 [21]) could detect an almost completely dark object ($\rho = 20$ %) at a maximum distance of 2 m within 50 µs, an object with a reflection index of 50 % at a maximum distance of 4.5 m within 150 µs, and an almost completely reflective object at a distance of even 10 m within 315 µs under extreme operating conditions described.

Table 1. Comparison of the performance achieved by three different InGaAs sensors under study in terms of the maximum measurable distance, standard deviation of the measured distance (yielding spatial resolution of the system in each case), and the minimum integration time required to generate a photosignal above the system noise level, at different reflection indices of the objects in the illuminated scene, and a background illumination of 100 klux if a narrow band pass filter (1550 ± 6 nm) is used.

Reflection index, ρ [%]	*Hamamatsu* G9201-256SB [19]		*Hamamatsu* G10768-1024D [20]		*Thorlabs* FGA015 [21]	
	Max. measurable distance, d_{max} [m]	Min. req. integration time, T_{int} [µs]	Max. measurable distance, d_{max} [m]	Min. req. integration time, T_{int} [µs]	Max. measurable distance, d_{max} [m]	Min. req. integration time, T_{int} [µs]
20	1.8	900	2.2	70	2	50
50	4.3	1.5×10^3	4.5	250	4.5	150
80	9.4	2.2×10^3	10	450	10	315

As explained before, the main purpose of proposing a hyperspectral imaging and ranging system for UGVs or UFVs is the possibility of using the SPI generated spatial information, delivered in form of a video-stream for decision making in continuous time with an acceptable frame-speed of at least 24 (ideally 33) fps. The latter implies: (1) reconstructing a 2D image out of the least possible amount of *Hadamard* illumination patterns projected by the array of LEDs, which means capturing these signals once they had reached the objects in the illuminated scene, got reflected by them, and reached the InGaAs sensor located aside the LEDs, and (2) processing all these photodetector photogenerated output voltage signals to reconstruct the 2D image. As reported in [22], we propose using 64 *Hadamard* patterns to generate a 2D SPI image with 64 ×16 virtual pixels, reaching a minimum processing time achievable of 13 ms for 2D image processing with a GPU based 4 kernel parallel architecture. For generated and detect 64 *Hadamard* illumination patterns, considering the results obtained for the *Thorlabs* FGA015 [21] sensor, the system would require 20.16 ms for objects in the scene at 10 m distance having 80 % reflectivity at full-sun background conditions; it would require 9.6 ms for objects

with a reflectivity of 50 % at 4.5 m depth, and 3.2 ms to depict almost completely dark objects at 2 m distance. Each individual pixel of the *Hamamatsu* G10768-1024D [20] line-sensor, would require 28.8 ms for 10 m distances of objects with 80 % reflectivity, 16 ms for objects placed at 4.5 m with 50 % reflectivity, and 4.48 ms for almost completely dark objects placed within 2 m distance from the sensor. Considering the calculations made, and the processing time of 13 ms required [22], the system using the *Thorlab* single InGaAs photodiode would be able to correctly detect and process information generating a video stream of between 30.16 and 65.8 fps. The *Hamamatsu* G10768-1024D [20] line-sensor, expanding the field of view 1024 times in one direction, would be enabling the production of video-streams of between 24 to 57.2 fps. Either way, the main goal of the proposed approach would be accomplished.

3. RADAR SYSTEM

Due to the advantages offered by orthogonal frequency-division multiplexing (OFDM) radars in terms of bandwidth, controlled in these systems using multiple-carriers, and in terms of ambiguity over LFM modulation [1], we propose using an OFDM radar imaging system with an operation frequency of 2.8 GHz together with the Software Defined Radios (SDR) tool, ETTUS B200 modules, and an antenna array. The proposed radar system is implemented and was finally tested on an UGV following the configuration shown in Fig. 2. The developed radar system operates in combination with the UGV vehicle, using the parameters defined and listed in Table 2. During the driving process, the scene scan is performed in front of the vehicle, and the RADAR imaging information is obtained from the radio signals reflected from the (mostly metallic) surrounding objects. Using the gathered information, a 2D image is generated, on the one hand, along the *x*-axis following a "cross-range" mode, following Eq. (6) [23], where d_{max} is the distance to the object, λ the emitted radiation wavelength, and L_{eff} the effective length of the antenna used for the emitter. On the other hand, the "down-range" is generated along the *y*-axis, defined using Eq. (7) [23], where c is the speed of light, N_f the frequency number, and Δf the subcarrier spacing.
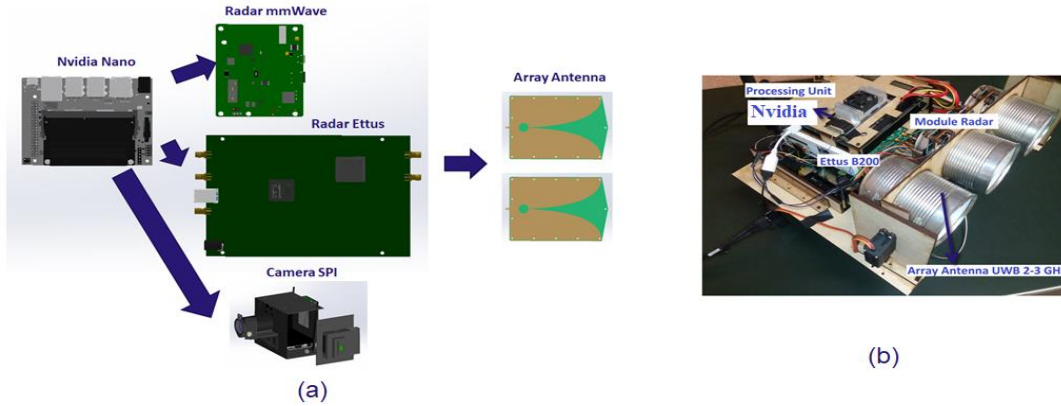

Figure 2. Schematic SPI-Radar systems, a) Control Nvidia Radar camera SPI , b) UGV test-vehicle carrying the proposed OFDM radar system.

$$\Delta x = \frac{d_{\max} \lambda}{2 L_{eff}} \tag{6}$$

$$\Delta y = \frac{c}{2 N_f \Delta f} \tag{7}$$

Table 2. The OFDM parameters used for the radar system proposed.

Symbol	Parameter	Value
fc	Carrier frequency	2-3 GHz
N_c	Number of subcarriers	64
M	Number of subsequent symbols	16
Δf	Subcarrier spacing	312.5 kHz
T_{ofdm}	OFDM period	3.6 μs
BW	Total signal bandwidth	500 MHz
r_{max}	Maximum unambiguous range	540 m
Δr	Range resolution	0.3 m
RCS	Radar Cross Section	$< 1 \, m^2$

The maximum Radar Cross-Section (RCS), σ_{max}, achievable by such a system can be determined using Eq. (8) [24], where d_{max} is once again the distance from the imaged object to the RADAR detector, h the object's height, and λ the emitted radiation wavelength.

$$\sigma_{\max} = \frac{2\pi d_{\max} h^2}{\lambda}$$

(8)

Once installed, for test purposes of the OFDM RADAR system, a test scenario was generated. During the first test, the system was able to detect a metallic cylindrical element having an 80 mm radius and a height of h = 114 mm, placed at a distance d_{max} = 90 cm from the UGV. In this case, the maximum RCS achieved by the system was of 0.025 m², as it can be observed in Fig. 3(a) on the final image on the right. In the second test scenario, as it can be observed in Fig. 3(b), we used two identical metallic cylindrical elements to test the system regarding its ability to discriminate nearby objects placed at relatively small distances apart, in this case 15 cm. The result suggests that the spatial resolution of the system under the circumstances used could be higher than 5 cm.
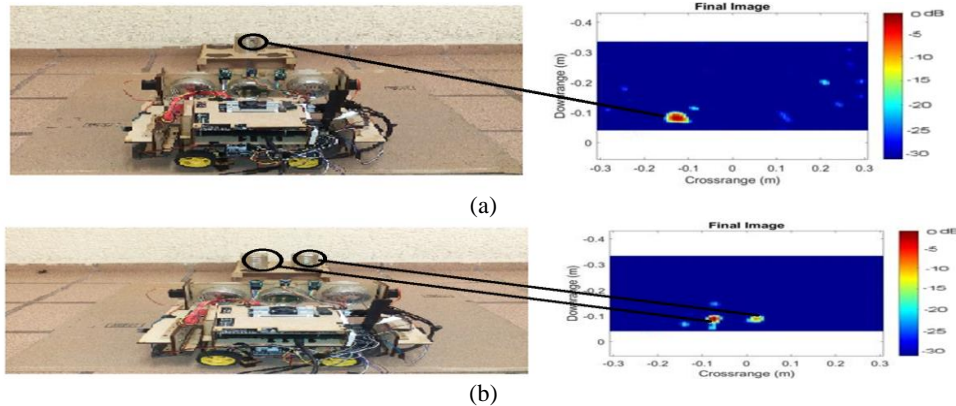

(a)

(b)

Figure 3. Photographs obtained from two test scenarios created for the performance evaluation of the OFDM RADAR system placed on top of an UGV (shown on both pictures on the left): (a) in the first test-scenario, a cylindrical metallic object was placed at a distance of 90 cm in front of the UGV, which was then properly imaged by the RADAR, as it can be shown on the graph on the right; (b) in the second test-scenario, two objects to the one used in (a) were placed at exactly the same spot but 15 cm apart from each other, and were once again properly imaged by the system, as shown on the graph on the right.

4. THE HYPERSPECTRAL HYBRID SPI-RADAR TEST SYSTEM PROPOSED

Based on the previous analyses, we propose using a hyperspectral hybrid SPI NIR system together with an OFDM RADAR system, as schematically shown in Fig. 4. The SPI stage consists of an active LED illumination system emitting NIR radiation with a wavelength of 1550 nm on the one side, and a detection stage consisting of a single InGaAs FGA015 photodiode and controller driver, on the other. In the radar stage, the use of the 80 GHz modulated frequency OFDM RADAR is proposed here, capable of reaching spatial resolutions of up to 37.5 mm and RCS values of between 10 and 50 m^2. The system proposed is designed to generated SPI images with virtual pixel resolutions of 64×64, 64×16, 128×16, or 256×16, yielding a compression factor of 3% and a spatial resolution (if ToF principle is additionally used) of < 1 mm. For the SPI image reconstruction, a Batch-OMP algorithm on 4-kernel parallel GPU platform [25] is used, reaching processing times of down to 13 ms [22], enabling in this way continuous-time decision making. The system must be constantly calibrated using a reference placed at a fixed distance from the system, which additionally enables RADAR imaging regardless of non-metallic obstacles, e.g. walls.
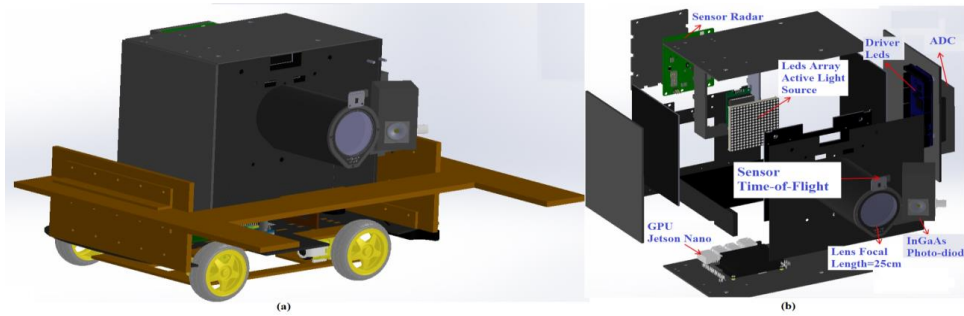

Figure 4. Proposed hyperspectral integrated vision system combining radar technology and NIR single-pixel optical principle for unmanned ground vehicles (UGV): a) a schematic representation of the proposed system on a test UGV; b) Schematic representation of the hybrid system showing the different elements that make up the SPI LED array, the LED driver electronics, the RADAR sensor, the InGaAs photodiode, and the GPU Jetson Nano platform.

CONCLUSION

To profit on the one side from the possibility offered by RADAR systems to detect mainly metal objects placed hundreds of meters from the detection system with positioning spatial resolutions in tens of centimeters; and expand this possibility by combining these systems with optical systems such as NIR SPI using 1550 nm wavelength active illumination, in this paper we propose and theoretically analyze the concept of a hyperspectral imaging system using a very low power consuming single commercially available InGaAs photodiode to generate 2D images and an array of NIR light emitting LEDs, combined with an 80 GHz millimeter band RADAR. The system is conceived to deliver a maximum radar range of 150 m with a maximum spatial resolution of ≤ 5 cm and a RADAR cross-section (RCS) of 10 – 50 m^2, combined with an optical system capable of generating at least 24 fps video streams based on SPI generated images yielding a maximum ranging depth of 10 m with a spatial resolution of < 1 cm. The proposed system will be used in unmanned ground vehicle (UGV) applications enabling decision making in continuous time.

REFERENCES

[1] Currie, N. C., Radar Reflectivity Measurement: Techniques and Applications. Norwood, MA, USA: Artech House, (1989).

[2] Ouyang, F. "ORTHOGONAL FREQUENCY DIVISION MULTIPLEXING (OFDM)" In *Digital Communication for Practicing Engineers*, F. Ouyang (Ed.) (2020). doi:10.1002/9781119598138.ch10

[3] Shahian Jahromi B, Tulabandhula T, Cetin S. Real-Time Hybrid Multi-Sensor Fusion Framework for Perception in Autonomous Vehicles. Sensors (Basel). 2019;19(20):4357. Published 2019 Oct 9. doi:10.3390/s19204357

[4] Lange R., Böhmer S., Buxbaum B. "11 - CMOS-based optical time-of-flight 3D imaging and ranging", in *High-Performance Silicon Imaging. Fundamentals and applications of CMOS and CCD sensors*, 2nd Edition, Ed. Daniel DURINI, *Elsevier*, UK, pp. 319 – 377 (2020) https://doi.org/10.1016/B978-0-08-102434-8.00011-8

[5] D. Stoppa et al., "A CMOS 3-D imager based on single photon avalanche diode", *IEEE Trans. Circuits Syst. I*, Reg. Papers, vol. 54, no. 1, pp. 4–12 (Jan., 2007)

[6] Neal R., Steven D. J., Matthew P.E., Catherine F. H., Robderick M. S. and Miles J. P., "Deep Learning optimized single-pixel LiDAR", Appl. Phys. Lett. 115,231101 (2019)

[7] https://www.osha.gov/dts/osta/otm/otm_iii/otm_iii_6.html, last visited on April 13, 2020

[8] Angelini, F., Colao, F. Optimization of laser wavelength, power and pulse duration for eye-safe Raman spectroscopy. *J. Eur. Opt. Soc.-Rapid Publ.* **15,** 2 (2019). https://doi.org/10.1186/s41476-019-0099-y

[9] Vaida V., Daniel J. S., Kjaergaard H. G., Goss L. M., Tuck A. F., "Atmospheric absorption of near infrared and visible solar radiation by the hydrogen bonded water dimer", *Quarterly Journal of the Royal Meteorological Soc.* Vol.127, Issue 575, July 2001 Part A, pp. 1627-1643

[10] Sze S. M. *Semiconductor Devices. Physics and Technology*, 2nd edn., John Wiley & Sons, Inc., USA (2002)

[11] https://www.hamamatsu.com/resources/pdf/ssd/ingaas_kird0005e.pdf, last visited on April 13, 2020

[12] M. P. Edgar, G. M. Gibson and M. J. Padgett "Principles and prospects for single-pixel imaging", *Nature Photon* 13, 13–20 (2019) https://doi.org/10.1038/s41566-018-0300-7

[13] M. Rani, S. B. Dhok and R. B. Deshmukh "A Systematic Review of Compressive Sensing: Concepts, Implementations and Applications," in *IEEE Access*, vol. 6, pp. 4875-4894 (2018)

[14] J. Tropp and A. Gilbert "Signal recovery from random measurements via orthogonal matching pursuit", *IEEE Transactions on Information Theory*, 53(12):4655-4666 (2007)

[15] https://www.osa-opto.com/smd-leds/eold-1550-525.html, last visited on April 16, 2020

[16] https://www.thorlabs.com/newgrouppage9.cfm?objectgroup_id=1000&pn=FB1550-30, last visited on April 16, 2020

[17] Kodak, 2008. *Kodak Fundamental Radiometry and Photometry. CCD Image Sensors*. Revision 2.0 MTD/PS-0891, 24 November.

[18] Süss, A. High Performance CMOS Range Imaging, Ph.D. Thesis, University of Duisburg-Essen, Duisburg, DU, (2014).

[19] https://www.hamamatsu.com/resources/pdf/ssd/g9201-256s_etc_kmir1012e.pdf, last visited on April 16, 2020

[20] https://www.hamamatsu.com/us/en/product/type/G10768-1024D/index.html, last visited on April 16, 2020

[21] https://www.thorlabs.com/drawings/81f5d67ac770a85d-F8FFE6E4-C89D-5897-6DA081C2A332A5AB/FGA015-SpecSheet.pdf, last visited on April 16, 2020

[22] Osorio Quero C., Durini D., Ramos-Garcia R., Rangel-Magdaleno J., Martinez Carranza J. "Hardware Parallel Architecture proposed to accelerate the Orthogonal Matching Pursuit Compressive Sensing Reconstruction", Proc. of the *SPIE Defense + Commercial Sensing 2020*, Digital Forum, 27 April - 1 May 2020, in press

[23] Hsueh-Jyh,L.and Yean-Woei, K., *The Electrical Engineering Handbook*, *Elsevier*, pp. 671-690 (2005)

[24] Tice, T. E., "An overview of radar cross section measurement techniques," *IEEE Transactions on Instrumentation and Measurement*, Vol. 39, pp. 205-207 (1990)

[25] Kulkarni A., and Mohsenin T. "Accelerating compressive sensing reconstruction omp algorithm with cpu, gpu, fpga and domain specific many-core," in *IEEE International Symposium on Circuits and Systems* ISCAS, pp. 970–973, (2015)